Advanced Raman Spectroscopy of $Cs_2AgBiBr_6$ Double Perovskites and Identification of $Cs_3Bi_2Br_9$ Secondary Phases

Paul Pistor[1,2], Michaela Meyns[2,#], Maxim Guc[2], Hei-Chen Wang[1], Miguel A.L. Marques[1],*

Xavier Alcobé[3], Andreu Cabot[2,4], Victor Izquierdo-Roca[2]

1 Martin-Luther-Universität Halle-Wittenberg, 06120 Halle (Saale), Germany

2 IREC - Catalonia Institute for Energy Research, 08930 Sant Adria de Besos, Spain

3 Centres Científics i Tecnològics, Universitat de Barcelona, 08028 Barcelona, Spain

4 ICREA -Institució Catalana de Recerca i Estudis Avançats, Barcelona, Spain.

Current adress: AWI – Alfred-Wegner-Institute Helmholtz Centre for Polar and Marine Research, 27498 Helgoland, Germany

Double Perovskite, $Cs_2AgBiBr_6$, Raman modes, secondary phase detection, Cs_3BiBr_9.

ABSTRACT $Cs_2AgBiBr_6$ double perovskites are intensely investigated as lead-free, stable alternatives to organic lead halide perovskites. In this contribution, we revise the vibrational modes of $Cs_2AgBiBr_6$ and show that Raman spectroscopy is well suited for the detection of common secondary phases such as $Cs_3Bi_2Br_9$. The combined Raman analysis at pre-, near- and non-resonant conditions allows us to extract the four vibrational modes of $Cs_2AgBiBr_6$ to unprecedented detail, the most intense one at 177.3 cm^{-1}. The experimental results are in good agreement with theoretical density functional theory calculations. In addition, we monitor the decomposition of $Cs_2AgBiBr_6$ into $Cs_3Bi_2Br_9$ at temperatures above 255°C.

During the last decade, their unique opto-electronic properties[1] enabled a fulminant parade of organic-inorganic lead halide perovskites in a variety of opto-electronic applications such as solar cells, photodetectors, X-ray detectors, light emitting diodes, etc. [2, 3, 4, 5] Yet, the implication of the toxic heavy metal Pb as well as their instability to moisture, UV-light and thermal stress have so far impeded commercial exploitation.[6, 7, 8] Considerable research interest is therefore currently put into the investigation of lead-free,[9, 10, 11] intrinsically more stable (perovskite) materials with similar opto-electronic properties.[12, 13, 14]

Perovskite materials in general have the generic formula ABX_3. In the $(Cs,FA,MA)Pb(I,Br,Cl)_3$ perovskite materials considered here, X is a halide (I, Br, Cl), B is lead and A is an organic molecule such as methyl ammonium (MA), formamidinium (FA) or a large inorganic atom such as Cs. In general, inorganic (Cs-based) perovskites are reported to be thermally more stable than their organic (MA-based) counterparts.[15, 16, 17] Homovalent substitution of Pb with Sn is possible, but the resulting tin-based materials are even less stable. Other more stable lead-free homovalent Pb substitutions with similar opto-electronic properties have not been found in vast theoretical screening of possible candidates.[18] McClure et al. suggested the double perovskite $Cs_2AgBiBr_6$ as a lead-free and more stable substitute for $MAPbI_3$, and successfully synthesized this compound from a solid-state and a solution route. They determined the band gap experimentally to be indirect at 2.19 eV,[19] which is supported by theoretical calculations.[20] An improved stability of $Cs_2AgBiBr_6$ against thermal decomposition[21] and to ambient air[19] has been reported. An intense and on-going research is producing very promising advances applying $Cs_2AgBiBr_6$ in high-sensitivity and air-stable photodetectors,[22, 23, 24] or photocatalysis.[25] The sufficiently large band-gap and the heavy elements involved turn $Cs_2AgBiBr_6$ also into an efficient and air-stable X-ray detector.[26, 27] . For example, Steele et al. reported highly sensitive X-ray detectors based on $Cs_2AgBiBr_6$ single crystals with long charge carrier lifetimes exceeding 1.5 µs and a sensitivity of 316 $\mu CGy^{-1}cm^{-2}$.[28] Yang et al. were already able to produce passivated $Cs_2AgBiBr_6$ wafers that enabled highly sensitive, low-noise X-ray imaging with good spatial resolution.[29]

This stimulates further characterization of structural and opto-electronic properties in view of luminescent and other semiconductor applications. The compositional stability range is rather narrow,[30] and several binary and ternary secondary phases have been reported.[24, 31, 32] Raman spectroscopy is a non-destructive and fast tool to control phase purity and monitor the undesired, uncontrolled appearance of secondary phases.[33] In this contribution, we therefore revise the Raman modes of the double perovskite $Cs_2AgBiBr_6$ in detail and show how Raman can be used to detect the most common secondary phase $Cs_3Bi_2Br_9$.

$Cs_2AgBiBr_6$ crystallizes in a cubic elpasolite (K_2NaAlF_6) crystal structure at room temperature (space group $Fm\bar{3}m$, a = 11.264 Å) resembling a double perovskite crystal structure.[20, 34] The structure is derived from the conventional perovskite structure ABX_3 (e.g. $CsPbI_3$) by heterovalent substitution of the B atom, i.e. substituting two divalent B cations (Pb) by one monovalent metal cation M^+ (Ag) and by one trivalent cation M^{3+} (Bi). This substitution leads to the generic formula

$A_2M^+M^{3+}X_6$, where in this crystal structure the M^+ (Ag) and M^{3+} (Bi) cations are ordered in a rock-salt configuration. An illustration of the crystal structure is depicted in figure 1 b). Other possible cesium halide double perovskites arise from the combination of other monovalent ($M^+ = Cu^+$, Ag^+, Au^+...) and trivalent cations ($M^{3+} = Bi^{3+}$, Sb^{3+}, In^{3+}...), some of which have been theoretically investigated in references [34] and [35].

Based on this generic double perovskite structure, the atomic positions are listed in table 1, together with the derived irreducible representations. These symmetry considerations predict four active Raman modes, namely one A_{1g}, one E_g and two F_{2g} modes.

Table 1: Wyckoff positions, symmetry and the associated irreducible representation for the atoms in the double perovskite $Cs_2AgBiBr_6$ phase with cubic structure, space group $Fm\bar{3}m$.

Atom	Wyckoff position	Symmetry	Irreducible representation
Cs	8*c*	O_h	F_{1u}
Ag	4*a*	O_h	F_{1u}
Bi	4*b*	T_d	$F_{1u} \oplus F_{2g}$
Br	24*e*	C_{4v}	$A_{1g} \oplus E_g \oplus F_{1g} \oplus 2F_{1u} \oplus F_{2g} \oplus F_{2u}$

		Modes classification	
IR	Raman	Acoustic	Silent
$4F_{1u}$	$A_{1g} \oplus E_g \oplus 2F_{2g}$	F_{1u}	$F_{1g} \oplus F_{2u}$

In the next step, we applied *ab initio* density functional theory to calculate the expected positions of these four Raman modes. Norm-conserving pseudopotentials and the local density approximation (LDA) to the exchange-correlation functional as implemented in the ABINIT code[36, 37, 38, 39] were used for this. The calculated electron and phonon band structures can be found in Figure 1 a) and c), respectively. The calculated electronic band structure confirms the indirect nature of the band gap. The calculated frequencies of the fundamental vibrational Raman active modes are collected in the table 2, and illustrations of the corresponding vibrational eigenmodes can be found in the supporting information. The main mode (A_{1g}), can be considered a breathing mode involving only the 6 Br atoms moving towards and away from the central Ag atom. The E_g mode is similar, but with 3 Br atoms moving towards the Ag atom, and 3 away from it at the same time. In mode $F_{2g}^{(1)}$, Cs atoms start moving in addition to Br, while in $F_{2g}^{(2)}$ all atoms are involved in the vibration.

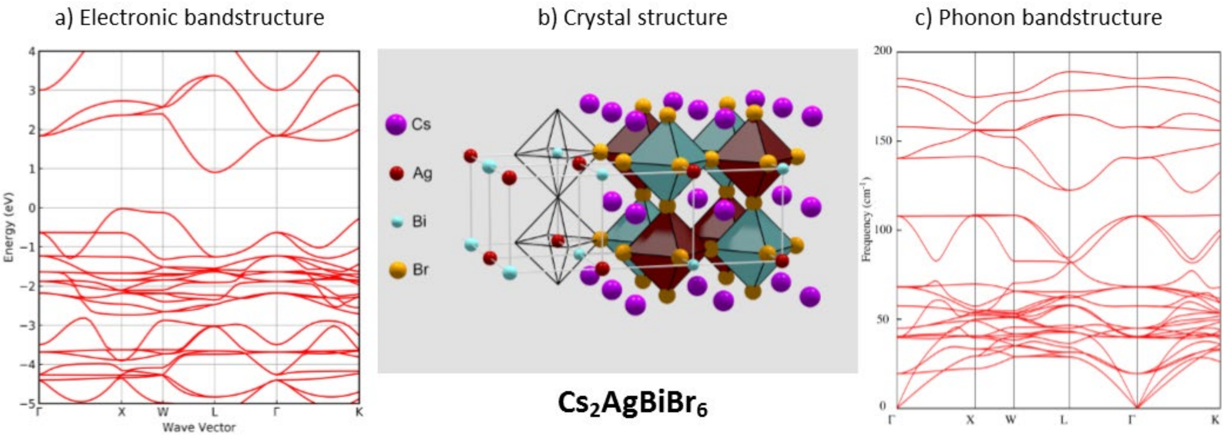

Figure 1 a) Calculated electron band structure of the double perovskite $Cs_2AgBiBr_6$. b) Sketch of the elpasolite crystal structure of $Cs_2AgBiBr_6$. c) Calculated phonon band structure of $Cs_2AgBiBr_6$.

In this work, we investigate two types of crystals by detailed analysis of their Raman spectra. Both crystals (type A and type B) were precipitated from an aqueous precursor solution by slow temperature induced single crystal growth following the route described by Slavney et al.[21] with nearly identical growth conditions, but marginally lower AgBr concentration for the type B crystals (see the supporting information (SI) for experimental details).

The first crystal (type A) is homogenous with dark orange color and large facets as fotographed in the inset of figure 2 a). Our phase analysis confirmed this type A crystal to be essentially phase pure $Cs_2AgBiBr_6$: X-ray fluorescence spectroscopy (XRF) revealed near stoichiometric $Cs_2AgBiBr_6$ composition for this crystal and X-ray diffraction (XRD) analysis confirmed the elpasolite-type crystal structure of $Cs_2AgBiBr_6$ with space group $Fm\bar{3}m$ (figure 2 a)). A complete Rietveld refinement yielded a lattice constant of a = 11.27317 Å (details may be found in the supporting information (SI)). A Kubelka-Munk plot (figure S2 of the SI) of the diffuse reflectance of these crystals revealed an indirect bandgap of 2.12 eV, in accordance with literature.[40]

The second crystal (type B) was inhomogeneous, dominated by a bright-yellow bulk color with large darker orange inclusions (figure 2 b)). In this case XRF measurements on the yellow regions indicate the absence of the Ag and a Cs:Bi:Br composition of close to 2:3:9. XRD measurements of ground powder samples of this type B crystals revealed phase mixtures of $Cs_2AgBiBr_6$ and a hexagonal crystal phase with space group $P\bar{3}m1$ and lattice constants a = 7.96026 Å, c = 9.84647 Å. The latter phase is identified as hexagonal $Cs_3Bi_2Br_9$, a layered form of a vacancy-ordered perovskite (ICDD PDF data entry 4-10-2676)[41] which has a direct band gap of 2.65 eV.[42]

Please note that the most intense XRD peaks of this hexagonal $Cs_3Bi_2Br_9$ phase overlap with peaks of the double perovskite $Cs_2AgBiBr_6$. These nearly coinciding peaks are marked with red-blue circles in figure 2 b). The detection of $Cs_3Bi_2Br_9$ traces in a $Cs_2AgBiBr_6$ matrix will therefore rely on less intense peaks which means that high quality diffractograms with long measurement times will be necessary for a clear distinction of the two phases in XRD.

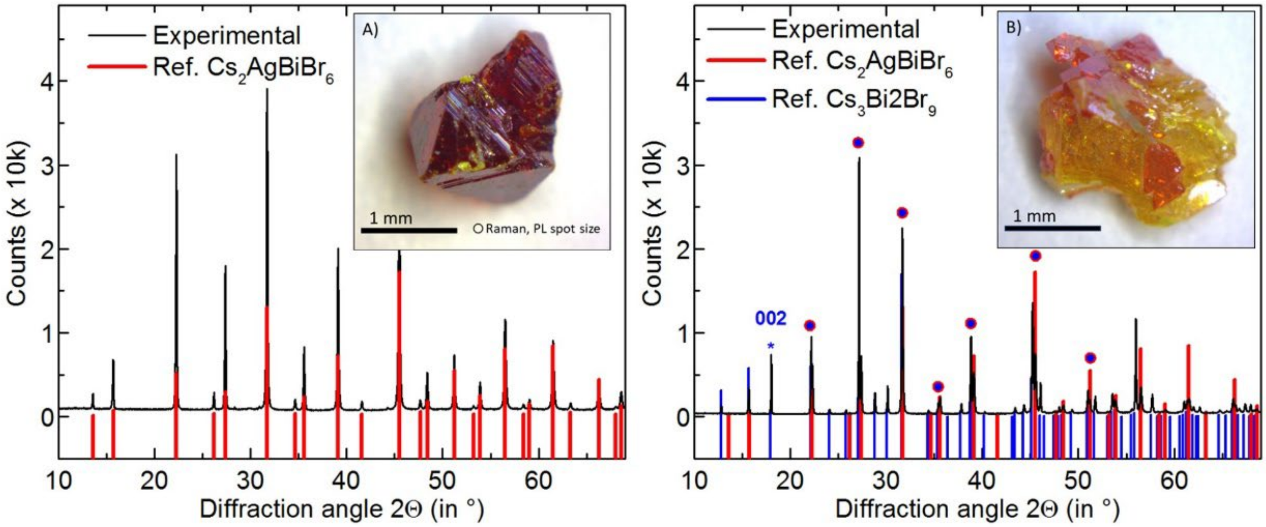

Figure 2: X-ray diffractograms of the two crystal types analyzed in this work. Left: Dark orange Type A crystals, which consist of phase pure $Cs_2AgBiBr_6$. Right: Inhomogeneous Type B crystals consisting of a mixture of $Cs_2AgBiBr_6$ and $Cs_3Bi_2Br_9$. The insets show photographs of respective single crystals.

For the experimental Raman analysis, laser light with four different wavelengths above and below the (indirect) optical band gap energy of $Cs_2AgBiBr_6$, was used as excitation source. This allows the characterization of the material in non-resonant (488 nm), pre-resonant (532 and 785 nm), and resonant (633nm) conditions with respect to the dominant optical absorption onset at 2.12 eV. We would like to remark that in contrast to common organic perovskites such as $MAPbI_3$, no laser-induced degradation was observed for the $Cs_2AgBiBr_6$ single crystals during the laser exposure while measuring with these excitation wavelengths, in accordance with previously published results for this material based on thin film samples.[22-24] Figure 3 shows the Raman spectra under these excitation conditions. Six Raman peaks can be observed, whose exact positions are collected in table 2 and have been extracted with the simultaneous fitting methodology reported by Dimitrievska et al.[33]

We observe a good agreement of our experimental data with the theoretical prediction, especially for the higher wavenumbers, which allows us to assign each peak to the specific symmetry (Table 2). The observed Raman modes are also in agreement with previously reported data, which are added to table 2 for comparison. The highest discrepancy in the Raman peaks frequency between our experimental and theoretical results, and data published in Ref. [43] was related to the $F_{2g}^{(1)}$ mode, which calculation and and previously published data locate close to 40 cm^{-1}, while in our spectra it is observed at 60.3 cm^{-1} (see table 2). The spectra excited with 488 nm excitation were recorded using a high resolution triple monochromator which allows approaching the laser line down to 20 cm^{-1}. With these conditions, (and in contrast to results from Ref. [43]) we would be easily able to identify any peaks close to 40 cm^{-1}, which was not the case in our measurements. However, a clear shoulder was observed at 60.3 cm^{-1}, which we assigned to the $F_{2g}^{(1)}$ symmetry mode consequently. Moreover, and the aforementioned shoulder was also clearly observed in the spectra measured with 532 nm excitation wavelength using another filter-based monochromator (see SI for more details). In this combination, we do not have any doubts of the existence of the peak at 60.3 cm^{-1} in a phase pure $Cs_2AgBiBr_6$ compound, although these results differ from previously published and theoretically calculated values and encourage a more detailed study on the nature of this peak.

Together with the four fundamental one-phonon peaks, we observed multi-phonon peaks at 344.3 and 518.2 cm^{-1}, which corresponds to the second and third order of the A_{1g} mode at 177.3 cm^{-1}, respectively. The small discrepancy (10 – 13 cm^{-1}) with respect to the expected position of the higher overtones can be explained by a strong anharmonicity in the atomic vibrations due to energies involved in the overtones that are far from the parabolic approximation of the interatomic potential energy.[44] A strong anharmonicity of this material has already been discussed in the context of large Stokes energy shifts and large emission line widths.[43] The intensity of the multi-phonon peaks is generally expected to be highest under the resonant conditions, when the excitation wavelength is close to the fundamental optical transitions, which in our case corresponds to 633 nm excitation. However, due to the indirect nature of band gap of $Cs_2AgBiBr_6$ a resonant effect became more pronounced when approaching the direct transition at the Γ-point of the Brillouin zone, which in this case has an energy of 2.6 eV (see SI) and is close to the energy of laser line at 488 nm (~2.54 eV). The better coupling with blue lasers was also observed by the authors in Ref. [43].

Additionally, the relative peak intensities are clearly modified by changing the excitation wavelengths (Fig. 3). For instance, there is a clear increase of the A_{1g} peak for lower excitation wavelengths in comparison to the intensity of other peaks. This is related to strong electron−phonon Fröhlich interactions within $Cs_2AgBiBr_6$ for the longitudinal A_{1g} mode.[43]

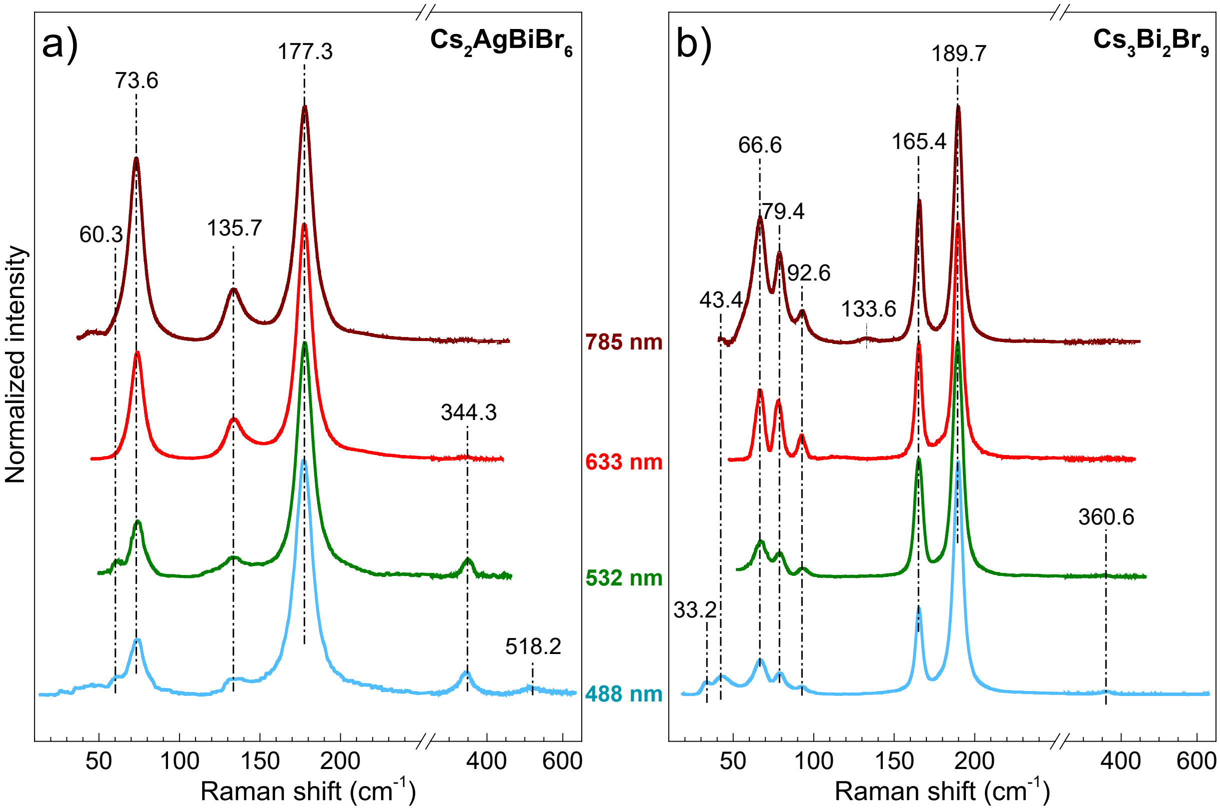

Figure 3: Raman spectra of the dark orange cubic $Cs_2AgBiBr_6$ double perovskite phase (type A) and the bright yellow hexagonal $Cs_3Bi_2Br_9$ phase (type B) measured with different excitation wavelengths.

Table 2: Experimentally determined Raman shifts and comparison to theoretical prediction and reference data for the $Cs_2AgBiBr_6$ double perovskite and the hexagonal $Cs_3Bi_2Br_9$ secondary phase.

$Cs_2AgBiBr_6$

This work	Ref. [43]	Theor. cal.	Symm.
60.3	40	40.31	$F_{2g}^{(1)}$
73.6	75	68.22	$F_{2g}^{(2)}$
135.7	135	140.34	E_g

$Cs_3Bi_2Br_9$

This work	Ref [45, 46]	Symm. [46]
33.2	27/30	
43.4	37/40	
66.6	63/65	

177.3	175	180.66	A_{1g}	79.4	76/78	
				92.6	91/89	
344.3			2×A_{1g}	133.6		
518.2			3×A_{1g}	165.4	167/167	A_{1g}
				189.7	192/191	E_g
				360.6		

We now turn to the inhomogeneous type B crystal, which according to the phase analysis consist of a mixture of the $Cs_2AgBiBr_6$ double perovskite phase and the hexagonal $Cs_2Bi_3Br_9$ phase. At the dark orange locations, identical Raman spectra corresponding to $Cs_2AgBiBr_6$ as reported above were observed. The very different Raman spectra at the yellow light phase regions are displayed in figure 2 b). The simultaneous deconvolution of the four Raman spectra results in 9 peaks (table 2), with the principal peak positions showing good agreement to the literature values for $Cs_2Bi_3Br_9$.[46] [45] However, the use of multiple excitation wavelengths greatly enhanced the sensitivity for several minor peaks, which have not been reported for this phase hitherto. For the hexagonal $Cs_2Bi_3Br_9$ with space group $P\bar{3}m1$, nine fundamental Raman active modes can be expected (four A_{1g} and five E_g), just as derived from our experiments. Valakh et al. were able to assign only the most intense modes at 165.4 cm^{-1} and 189.7 cm^{-1} to A_{1g} and E_g symmetry, respectively, while the other modes remained unclear.[46] These assignments were confirmed by theoretical calculations of Kentsch et al.[47]

To summarize, we find that $Cs_2AgBiBr_6$ shows sharp and intense Raman peaks at a variety of excitation conditions. This is in contrast to $MAPbI_3$, which was found to be prone to degradation upon laser excitation and offers only rather broad Raman features similar to the ones of PbI_2.[48] Furthermore, the peaks of $Cs_2AgBiBr_6$ are clearly distinguished from the sharp Raman peaks of the most common secondary phase $Cs_3Bi_2Br_9$, which readily formed during our crystal synthesis. This makes Raman spectroscopy very useful for the analysis of phase purity and the detection of secondary phases in this kind of double perovskite materials. With this in mind, we had a closer second look at the type A crystal and could identify very small traces of a $Cs_3Bi_2Br_9$ secondary phase at some edge even for this crystal, undetected by other measurement techniques.

Finally, we investigate the thermal decomposition and placed an $Cs_2AgBiBr_6$ type A crystal repeatedly for 5 min. on a hot plate (in air), whose temperature was increased stepwise from 35 °C to 275°C. Its Raman spectrum was recorded with 633 nm excitation wavelength after each temperature step (figure 4). No variation of the Raman spectra was observed up to 225 °C, confirming the enhanced thermal stability of this inorganic double perovskite. At higher temperatures, the main peaks of $Cs_3Bi_2Br_9$ at 165.4 cm^{-1} and 189.7 cm^{-1} can clearly be distinguished. This evidences degradation of the double perovskite $Cs_2AgBiBr_6$ into $Cs_3Bi_2Br_9$ at temperatures above 250 °C (in air). The onset of decomposition can be more clearly identified by inspecting the full width at half maximum (FWHM) of the main A_{1g} mode of $Cs_2AgBiBr_6$ (inset figure 4), which sharply increase at a temperature of 255 °C and above.

The final edited work is published at: https://doi.org/10.1016/j.scriptamat.2020.03.040.

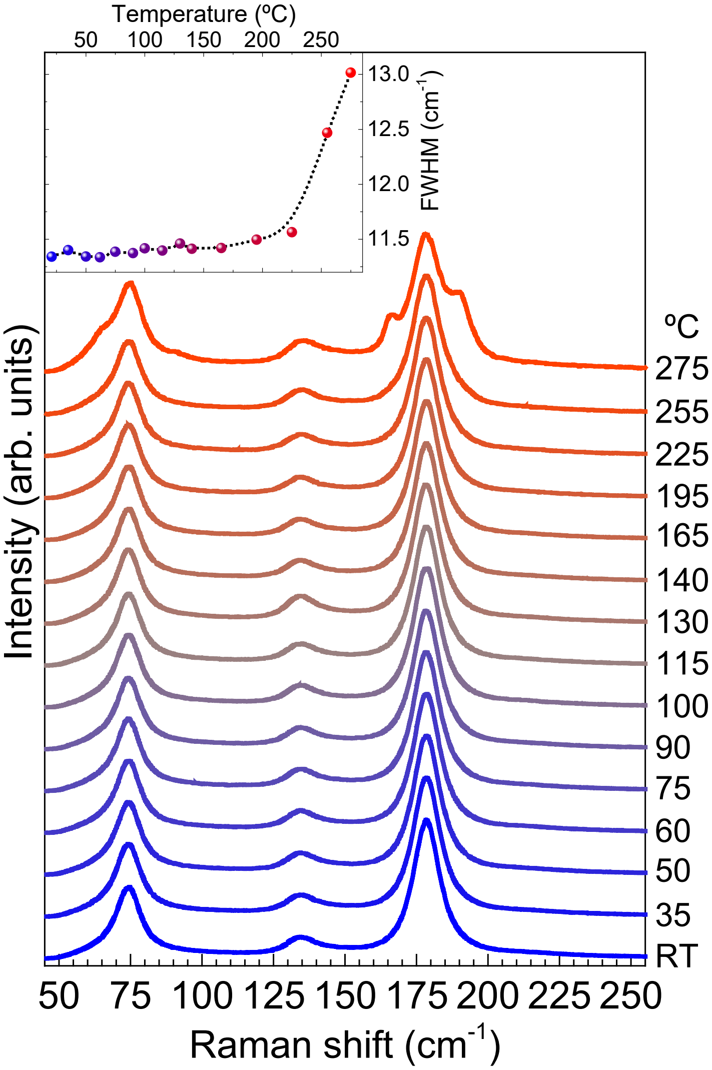

Figure 4: Evolution of the Raman spectra of a $Cs_2AgBiBr_6$ crystal (type A) during thermal decomposition on a hot plate, measured with an excitation wavelength of 633 nm. Inset: Evolution of the full width at half maximum (FWHM) of the A_{1g} mode (177.3 cm^{-1}).

We revised the Raman modes of $Cs_2AgBiBr_6$ and identified four active modes by crosslinking group theory arguments, DFT predictions and experimental multi-wavelength Raman measurements of phase-pure $Cs_2AgBiBr_6$ single crystals. We accurately determined the positions of the $F_{2g}^{(1)}$, $F_{2g}^{(2)}$, E_g and the main A_{1g} mode to be at 60.3, 73.6, 135.7 and 177.3 cm^{-1}, respectively. We find large portions of a hexagonal $Cs_3Bi_2Br_9$ secondary phase for inhomogeneous type B crystals, whose very distinct Raman features are also analyzed and compared to $Cs_2AgBiBr_6$. With Raman spectroscopy, we are able to detect the thermal decomposition of $Cs_2AgBiBr_6$ into $Cs_3Bi_2Br_9$ at temperatures above 250 °C, way above standard operation temperatures of opto-electronic devices. We offer precise reference values for the Raman analysis of $Cs_3Bi_2Br_9$ and $Cs_3Bi_2Br_9$ materials and show the potential of Raman spectroscopy to characterize these inorganic double halide perovskite materials and its sensitivity to detect secondary phases. With this, we help the development of high quality material synthesis and hope to foster further research on this promising lead-free and stable perovskite material family.

Supporting Information.

In the supporting information, details on the experimental methods and conditions as well as the theoretical DFT calculations can be found as well as additional data concerning the diffuse reflectance measurements and Rietveld refinement of the crystals. A schematic sketch of the four Raman active eigenmodes of $Cs_2AgBiBr_6$ are also included.

Acknowledgments

This research has received funding from the European Union's Seventh Framework Programme under grant agreement no. GA 625840 ("JumpKEST") and European Regional Development Founds (ERDF, FEDER, Programa Competitivitat de Catalunya 2007–2013). Authors from IREC belong to the M-2E (Electronic Materials for Energy) Consolidated Research Group and the XaRMAE Network of Excellence on Materials for Energy of the "Generalitat de Catalunya". The research leading to these results has received funding from MINECO (Ministerio de Economía y Competitividad de España) under the NASCENT project (ENE2014-56237-C4-1-R).

References

[1] R. E. Brandt, V. Stevanovic, D. S. Ginley, T. Buonassisi, Identifying defect-tolerant semiconductors with high minority-carrier lifetimes: beyond hybrid lead halide perovskites, MRS Communications 5 (2015) 265–275. https://doi.org/10.1557/mrc.2015.26 doi:10.1557/mrc.2015.26.

[2] S. Brittman, G. W. P. Adhyaksa, E. C. Garnett, The expanding world of hybrid perovskites: materials properties and emerging applications, MRC 5 (01) (2015) 7???26. https://doi.org/10.1557/mrc.2015.6 doi:10.1557/mrc.2015.6.

[3] L. M. Herz, Charge-carrier mobilities in metal halide perovskites: Fundamental mechanisms and limits, ACS Energy Letters 2 (7) (2017) 1539–1548. https://doi.org/10.1021/acsenergylett.7b00276 doi:10.1021/acsenergylett.7b00276.

[4] S. D. Stranks, H. J. Snaith, http://dx.doi.org/10.1038/nnano.2015.90Metal-halide perovskites for photovoltaic and light-emitting devices, Nature Nanotechnology 10 (5) (2015) 391–402. https://doi.org/10.1038/nnano.2015.90 doi:10.1038/nnano.2015.90. http://dx.doi.org/-10.1038/nnano.2015.90

[5] G. Wang, http://onlinepresent.org/proceedings/vol83_2015/13.pdfAn overview of photovoltaic and electronic-to-optical material based on perovskite, Advanced Science and Technology Letters 83 (2015) 66–70. https://doi.org/10.14257/astl.2015.83.13 doi:10.14257/astl.2015.83.13. http://onlinepresent.org/proceedings/vol83_2015/13.pdf

[6] T. A. Berhe, W.-N. Su, C.-H. Chen, C.-J. Pan, J.-H. Cheng, H.-M. Chen, M.-C. Tsai, L.-Y. Chen, A. A. Dubale, B.-J. Hwang, http://dx.doi.org/10.1039/c5ee02733kOrganometal halide

perovskite solar cells: degradation and stability, Energy Environ. Sci. 9 (2) (2016) 323–356. https://doi.org/10.1039/c5ee02733k doi:10.1039/c5ee02733k. http://dx.doi.org/10.1039/-c5ee02733k

[7] M. GrÃ¤tzel, The light and shade of perovskite solar cells, Nature Materials 13 (9) (2014) 838–842. https://doi.org/10.1038/nmat4065 doi:10.1038/nmat4065.

[8] T. Leijtens, K. Bush, R. Cheacharoen, R. Beal, A. Bowring, M. D. McGehee, Towards enabling stable lead halide perovskite solar cells interplay between structural, environmental, and thermal stability, J. Mater. Chem. A 5 (2017) 11483–11500. https://doi.org/10.1039/c7ta00434f doi:10.1039/c7ta00434f.

[9] S. F. Hoefler, G. Trimmel, T. Rath, Progress on lead-free metal halide perovskites for photovoltaic applications: a review, Monatshefte fÃ¼r Chemie - Chemical Monthly 148 (5) (2017) 795–826. https://doi.org/10.1007/s00706-017-1933-9 doi:10.1007/s00706-017-1933-9.

[10] H. Hu, B. Dong, W. Zhang, http://dx.doi.org/10.1039/C7TA00269FLow-toxic metal halide perovskites: opportunities and future challenges, J. Mater. Chem. A (2017) – https://doi.org/10.1039/C7TA00269F doi:10.1039/C7TA00269F. http://dx.doi.org/10.1039/-C7TA00269F

[11] Z. Shi, J. Guo, Y. Chen, Q. Li, Y. Pan, H. Zhang, Y. Xia, W. Huang, http://onlinelibrary.wiley.com/doi/10.1002/adma.201605005/abstractLead-free organicâ€“inorganic hybrid perovskites for photovoltaic applications: Recent advances and perspectives, Advanced Materials 29 (16) (2017) 1605005. https://doi.org/10.1002/adma.201605005 doi:10.1002/adma.201605005. http://-onlinelibrary.wiley.com/doi/10.1002/adma.201605005/abstract

[12] R. Wang, M. Mujahid, Y. Duan, Z.-K. Wang, J. Xue, Y. Yang, A review of perovskites solar cell stability, Advanced Functional Materials (2019) 1808843https://doi.org/10.1002/adfm.201808843 doi:10.1002/adfm.201808843.

[13] S. Yang, W. Fu, Z. Zhang, H. Chen, C.-Z. Li, http://dx.doi.org/10.1039/C7TA00366HRecent advances in perovskite solar cells: efficiency, stability and lead-free perovskite, J. Mater. Chem. A 5 (2017) 11462–11482. https://doi.org/10.1039/C7TA00366H doi:10.1039/C7TA00366H. http://dx.doi.org/10.1039/-C7TA00366H

[14] X.-G. Zhao, J.-H. Yang, Y. Fu, D. Yang, Q. Xu, L. Yu, S.-H. Wei, L. Zhang, Design of lead-free inorganic halide perovskites for solar cells via cation-transmutation, Journal of the American Chemical Society 139 (7) (2017) 2630–2638. https://doi.org/10.1021/jacs.6b09645 doi:10.1021/jacs.6b09645.

[15] T. Burwig, W. FrÃ¤nzel, P. Pistor, Crystal phases and thermal stability of co-evaporated CsPbX3 (x = i, br) thin films, Journal of Physical Chemistry Letters 9 (16) (2018) 4808–4813. https://doi.org/10.1021/acs.jpclett.8b02059 doi:10.1021/acs.jpclett.8b02059.

[16] M. Kulbak, S. Gupta, N. Kedem, I. Levine, T. Bendikov, G. Hodes, D. Cahen, Cesium enhances long-term stability of lead bromide perovskite-based solar cells, The journal of physical chemistry letters 7 (1) (2015) 167–172. https://doi.org/10.1021/acs.jpclett.5b02597 doi:10.1021/acs.jpclett.5b02597.

[17] P. Pistor, T. Burwig, C. Brzuska, B. Weber, W. FrÃ¤nzel, Thermal stability and miscibility of co-evaporated methyl ammonium lead halide (MAPbX3, x = i, br, cl) thin films analysed by in situ x-ray diffraction, Journal of Materials Chemistry A 6 (24) (2018) 11496–11506. https://doi.org/10.1039/c8ta02775g doi:10.1039/c8ta02775g.

[18] M. R. Filip, F. Giustino, Computational screening of homovalent lead substitution in organicinorganic halide perovskites, The Journal of Physical Chemistry C 120 (1) (2015) 166–173. https://doi.org/10.1021/acs.jpcc.5b11845 doi:10.1021/acs.jpcc.5b11845.

[19] E. T. McClure, M. R. Ball, W. Windl, P. M. Woodward, http://dx.doi.org/10.1021/acs.chemmater.5b04231Cs2agbix 6 (x = br, cl): New visible light absorbing, lead-free halide perovskite semiconductors, Chem. Mater. 28 (5) (2016) 1348–1354. https://doi.org/10.1021/acs.chemmater.5b04231 doi:10.1021/acs.chemmater.5b04231. http://-dx.doi.org/10.1021/acs.chemmater.5b04231

[20] M. R. Filip, S. Hillman, A. A. Haghighirad, H. J. Snaith, F. Giustino, http://dx.doi.org/10.1021/acs.jpclett.6b01041Band gaps of the lead-free halide double perovskites cs2biagcl6and cs2biagbr6from theory and experiment, The Journal of Physical Chemistry Letters 7 (13) (2016) 2579???2585. https://doi.org/10.1021/acs.jpclett.6b01041 doi:10.1021/acs.jpclett.6b01041. http://dx.doi.org/10.1021/acs.jpclett.6b01041

[21] A. H. Slavney, T. Hu, A. M. Lindenberg, H. I. Karunadasa, http://dx.doi.org/10.1021/jacs.5b13294A bismuth-halide double perovskite with long carrier recombination lifetime for photovoltaic applications, Journal of the American Chemical Society (Feb 2016). https://doi.org/10.1021/jacs.5b13294 doi:10.1021/jacs.5b13294. http://dx.doi.org/-10.1021/jacs.5b13294

[22] L.-Z. Lei, Z.-F. Shi, Y. Li, Z.-Z. Ma, F. Zhang, T.-T. Xu, Y.-T. Tian, D. Wu, X.-J. Li, G.-T. Du, High-efficiency and air-stable photodetectors based on lead-free double perovskite cs2agbibr6 thin films, Journal of Materials Chemistry C 6 (30) (2018) 7982–7988. https://doi.org/10.1039/c8tc02305k doi:10.1039/c8tc02305k.

[23] C. Wu, B. Du, W. Luo, Y. Liu, T. Li, D. Wang, X. Guo, H. Ting, Z. Fang, S. Wang, Z. Chen, Y. Chen, L. Xiao, Highly efficient and stable self-powered ultraviolet and deep-blue photodetector based on cs2 AgBiBr6 /SnO2 heterojunction, Advanced Optical Materials 6 (22) (2018) 1800811. https://doi.org/10.1002/adom.201800811 doi:10.1002/adom.201800811.

[24] J. Yang, C. Bao, W. Ning, B. Wu, F. Ji, Z. Yan, Y. Tao, J.-M. Liu, T. C. Sum, S. Bai, J. Wang, W. Huang, W. Zhang, F. Gao, Stable, high-sensitivity and fast-response photodetectors based on lead-free cs 2 AgBiBr 6 double perovskite films, Advanced Optical Materials (2019) 1801732https://doi.org/10.1002/adom.201801732 doi:10.1002/adom.201801732.

[25] Z. Zhang, Y. Liang, H. Huang, X. Liu, Q. Li, L. Chen, D. Xu, Stable and highly efficient photocatalysis with lead-free double-perovskite of cs2 AgBiBr6, Angewandte Chemie International Edition 58 (22) (2019) 7263–7267. https://doi.org/10.1002/anie.201900658 doi:10.1002/anie.201900658.

[26] W. Pan, H. Wu, J. Luo, Z. Deng, C. Ge, C. Chen, X. Jiang, W.-J. Yin, G. Niu, L. Zhu, L. Yin, Y. Zhou, Q. Xie, X. Ke, M. Sui, J. Tang, Cs2agbibr6 single-crystal x-ray detectors with a low detection limit, Nature Photonics 11 (11) (2017) 726–732. https://doi.org/10.1038/s41566-017-0012-4 doi:10.1038/s41566-017-0012-4.

[27] W. Yuan, G. Niu, Y. Xian, H. Wu, H. Wang, H. Yin, P. Liu, W. Li, J. Fan, In situ regulating the orderdisorder phase transition in cs 2 AgBiBr 6 single crystal toward the application in an x-ray detector, Advanced Functional Materials 29 (20) (2019) 1900234. https://doi.org/10.1002/adfm.201900234 doi:10.1002/adfm.201900234.

[28] J. A. Steele, W. Pan, C. Martin, M. Keshavarz, E. Debroye, H. Yuan, S. Banerjee, E. Fron, D. Jonckheere, C. W. Kim, W. Baekelant, G. Niu, J. Tang, J. Vanacken, M. V. der Auweraer, J. Hofkens, M. B. J. Roeffaers, Photophysical pathways in highly sensitive cs2 AgBiBr6 double-

perovskite single-crystal x-ray detectors, Advanced Materials 30 (46) (2018) 1804450. https://doi.org/10.1002/adma.201804450 doi:10.1002/adma.201804450.

[29] B. Yang, W. Pan, H. Wu, G. Niu, J.-H. Yuan, K.-H. Xue, L. Yin, X. Du, X.-S. Miao, X. Yang, Q. Xie, J. Tang, Heteroepitaxial passivation of cs2agbibr6 wafers with suppressed ionic migration for x-ray imaging, Nature Communications 10 (1) (apr 2019). https://doi.org/10.1038/s41467-019-09968-3 doi:10.1038/s41467-019-09968-3.

[30] J. Breternitz, S. Levcenko, H. Hempel, G. Gurieva, A. Franz, A. Hoser, S. Schorr, Mechanochemical synthesis of the lead-free double perovskite cs2[AgIn]br6 and its optical properties, Journal of Physics: Energy 1 (2) (2019) 025003. https://doi.org/10.1088/2515-7655/ab155b doi:10.1088/2515-7655/ab155b.

[31] S. E. Creutz, E. N. Crites, M. C. D. Siena, D. R. Gamelin, Colloidal nanocrystals of lead-free double-perovskite (elpasolite) semiconductors: Synthesis and anion exchange to access new materials, Nano Letters 18 (2) (2018) 1118–1123. https://doi.org/10.1021/acs.nanolett.7b04659 doi:10.1021/acs.nanolett.7b04659.

[32] W. Ning, F. Wang, B. Wu, J. Lu, Z. Yan, X. Liu, Y. Tao, J.-M. Liu, W. Huang, M. Fahlman, L. Hultman, T. C. Sum, F. Gao, Long electron-hole diffusion length in high-quality lead-free double perovskite films, Advanced Materials 30 (20) (2018) 1706246. https://doi.org/10.1002/adma.201706246 doi:10.1002/adma.201706246.

[33] M. Dimitrievska, A. Fairbrother, E. Saucedo, A. PÃ©rez-RodrÃ-guez, V. Izquierdo-Roca, http://dx.doi.org/10.1016/j.solmat.2016.01.029Secondary phase and cu substitutional defect dynamics in kesterite solar cells: Impact on optoelectronic properties, Solar Energy Materials and Solar Cells 149 (2016) 304–309. https://doi.org/10.1016/j.solmat.2016.01.029 doi:10.1016/j.solmat.2016.01.029. http://dx.doi.org/10.1016/j.solmat.2016.01.029

[34] G. Volonakis, M. R. Filip, A. A. Haghighirad, N. Sakai, B. Wenger, H. J. Snaith, F. Giustino, http://dx.doi.org/10.1021/acs.jpclett.6b00376Lead-free halide double perovskites via heterovalent substitution of noble metals, The Journal of Physical Chemistry Letters 7 (7) (2016) 1254–1259. https://doi.org/10.1021/acs.jpclett.6b00376 doi:10.1021/acs.jpclett.6b00376. http://-dx.doi.org/10.1021/acs.jpclett.6b00376

[35] F. Wei, Z. Deng, S. Sun, F. Zhang, D. M. Evans, G. Kieslich, S. Tominaka, M. A. Carpenter, J. Zhang, P. D. Bristowe, A. K. Cheetham, Synthesis and properties of a lead-free hybrid double perovskite: (CH3nh3)2agbibr6, Chemistry of Materials 29 (3) (2017) 1089–1094. https://doi.org/10.1021/acs.chemmater.6b03944 doi:10.1021/acs.chemmater.6b03944.

[36] X. Gonze, A brief introduction to the ABINIT software package, Zeitschrift fÃ¼r Kristallographie - Crystalline Materials 220 (5/6) (2005) 558â€"–562. https://doi.org/10.1524/zkri.220.5.558.65066 doi:10.1524/zkri.220.5.558.65066.

[37] X. Gonze, J.-M. Beuken, R. Caracas, F. Detraux, M. Fuchs, G.-M. Rignanese, L. Sindic, M. Verstraete, G. Zerah, F. Jollet, M. Torrent, A. Roy, M. Mikami, P. Ghosez, J.-Y. Raty, D. Allan, First-principles computation of material properties: the ABINIT software project, Computational Materials Science 25 (3) (2002) 478–492. https://doi.org/10.1016/s0927-0256(02)00325-7 doi:10.1016/s0927-0256(02)00325-7.

[38] X. Gonze, B. Amadon, P.-M. Anglade, J.-M. Beuken, F. Bottin, P. Boulanger, F. Bruneval, D. Caliste, R. Caracas, M. Côté, T. Deutsch, L. Genovese, P. Ghosez, M. Giantomassi, S. Goedecker, D. Hamann, P. Hermet, F. Jollet, G. Jomard, S. Leroux, M. Mancini, S. Mazevet, M. Oliveira, G. Onida, Y. Pouillon, T. Rangel, G.-M. Rignanese, D. Sangalli, R. Shaltaf, M. Torrent, M. Verstraete, G. Zerah, J. Zwanziger, ABINIT: First-principles approach to material and nanosystem properties, Computer Physics Communications

180 (12) (2009) 2582–2615. https://doi.org/10.1016/j.cpc.2009.07.007 doi:10.1016/j.cpc.2009.07.007.

[39] X. Gonze, F. Jollet, F. A. Araujo, D. Adams, B. Amadon, T. Applencourt, C. Audouze, J.-M. Beuken, J. Bieder, A. Bokhanchuk, E. Bousquet, F. Bruneval, D. Caliste, M. Côté, F. Dahm, F. D. Pieve, M. Delaveau, M. D. Gennaro, B. Dorado, C. Espejo, G. Geneste, L. Genovese, A. Gerossier, M. Giantomassi, Y. Gillet, D. Hamann, L. He, G. Jomard, J. L. Janssen, S. L. Roux, A. Levitt, A. Lherbier, F. Liu, I. Lukacevic, A. Martin, C. Martins, M. Oliveira, S. Poncé, Y. Pouillon, T. Rangel, G.-M. Rignanese, A. Romero, B. Rousseau, O. Rubel, A. Shukri, M. Stankovski, M. Torrent, M. V. Setten, B. V. Troeye, M. Verstraete, D. Waroquiers, J. Wiktor, B. Xu, A. Zhou, J. Zwanziger, Recent developments in the ABINIT software package, Computer Physics Communications 205 (2016) 106–131. https://doi.org/10.1016/j.cpc.2016.04.003 doi:10.1016/j.cpc.2016.04.003.

[40] D. Bartesaghi, A. H. Slavney, M. C. Gélvez-Rueda, B. A. Connor, F. C. Grozema, H. I. Karunadasa, T. J. Savenije, Charge carrier dynamics in cs2agbibr6 double perovskite, The Journal of Physical Chemistry C 122 (9) (2018) 4809–4816. https://doi.org/10.1021/acs.jpcc.8b00572 doi:10.1021/acs.jpcc.8b00572.

[41] F. Lazarini, Caesium enneabromodibismuthate(III), Acta Crystallographica Section B Structural Crystallography and Crystal Chemistry 33 (9) (1977) 2961–2964. https://doi.org/10.1107/s0567740877009984 doi:10.1107/s0567740877009984.

[42] K. K. Bass, L. Estergreen, C. N. Savory, J. Buckeridge, D. O. Scanlon, P. I. Djurovich, S. E. Bradforth, M. E. Thompson, B. C. Melot, Vibronic structure in room temperature photoluminescence of the halide perovskite cs3bi2br9, Inorganic Chemistry 56 (1) (2016) 42–45. https://doi.org/10.1021/acs.inorgchem.6b01571 doi:10.1021/acs.inorgchem.6b01571.

[43] J. A. Steele, P. Puech, M. Keshavarz, R. Yang, S. Banerjee, E. Debroye, C. W. Kim, H. Yuan, N. H. Heo, J. Vanacken, A. Walsh, J. Hofkens, M. B. J. Roeffaers, Giant electronphonon coupling and deep conduction band resonance in metal halide double perovskite, ACS Nano 12 (8) (2018) 8081–8090. https://doi.org/10.1021/acsnano.8b02936 doi:10.1021/acsnano.8b02936.

[44] P. Yu, M. Cardona, Fundamentals of Semiconductors, 1999. https://doi.org/10.1007/978-3-662-03848-2 doi:10.1007/978-3-662-03848-2.

[45] G. Bator, J. Baran, R. Jakubas, M. Karbowiak, Raman studies of structural phase transition in cs3bi2br9, Vibrational Spectroscopy 16 (1) (1998) 11–20. https://doi.org/10.1016/s0924-2031(97)00041-6 doi:10.1016/s0924-2031(97)00041-6.

[46] M. Valakh, M. Lisitsa, E. Peresh, O. Trylis, A. Yaremko, The raman spectra of the family crystals cs3bi2br9, rb3bi2br9 and rb3sb2br9, Journal of Molecular Structure 436-437 (1997) 309–313. https://doi.org/10.1016/s0022-2860(97)00204-4 doi:10.1016/s0022-2860(97)00204-4.

[47] R. Kentsch, M. Scholz, J. Horn, D. Schlettwein, K. Oum, T. Lenzer, Exciton dynamics and electronphonon coupling affect the photovoltaic performance of the cs2agbibr6 double perovskite, The Journal of Physical Chemistry C 122 (45) (2018) 25940–25947. https://doi.org/10.1021/acs.jpcc.8b09911 doi:10.1021/acs.jpcc.8b09911.

[48] P. Pistor, A. Ruiz, A. Cabot, V. Izquierdo-Roca, http://dx.doi.org/10.1038/srep35973Advanced raman spectroscopy of methylammonium lead iodide: Development of a non-destructive characterisation methodology, Scientific Reports 6 (2016) 35973. https://doi.org/10.1038/srep35973 doi:10.1038/srep35973. http://dx.doi.org/-10.1038/srep35973